

## Article

# Lithium Tracer Diffusion in $\text{Li}_x\text{CoO}_2$ and $\text{Li}_x\text{Ni}_{1/3}\text{Mn}_{1/3}\text{Co}_{1/3}\text{O}_2$ ( $x = 1, 0.9, 0.65$ )-Sintered Bulk Cathode Materials for Lithium-Ion Batteries

Erwin Hüger<sup>1,2,\*</sup> , Daniel Uxa<sup>2</sup>  and Harald Schmidt<sup>1,2</sup> 

<sup>1</sup> Clausthal Center for Materials Technology, Clausthal University of Technology, 38678 Clausthal-Zellerfeld, Germany; harald.schmidt@tu-clausthal.de

<sup>2</sup> Solid State Kinetics Group, Institute of Metallurgy, Clausthal University of Technology, 38678 Clausthal-Zellerfeld, Germany; daniel.uxa@tu-clausthal.de

\* Correspondence: erwin.hueger@tu-clausthal.de

**Abstract:** The knowledge of Li diffusivities in electrode materials of Li-ion batteries (LIBs) is essential for a fundamental understanding of charging/discharging times, maximum capacities, stress formation and possible side reactions. The literature indicates that Li diffusion in the cathode material  $\text{Li}(\text{Ni},\text{Mn},\text{Co})\text{O}_2$  strongly increases during electrochemical delithiation. Such an increased Li diffusivity will be advantageous for performance if it is present already in the initial state after synthesis. In order to understand the influence of a varying initial Li content on Li diffusion, we performed Li tracer diffusion experiments on  $\text{Li}_x\text{CoO}_2$  (LCO) and  $\text{Li}_x\text{Ni}_{1/3}\text{Mn}_{1/3}\text{Co}_{1/3}\text{O}_2$  (NMC,  $x = 1, 0.9, 0.65$ ) cathode materials. The measurements were performed on polycrystalline sintered bulk materials, free of additives and binders, in order to study the intrinsic properties. The variation of Li content was achieved using reactive solid-state synthesis using pressed  $\text{Li}_2\text{CO}_3$ , NiO,  $\text{Co}_3\text{O}_4$  and/or  $\text{MnO}_2$  powders and high temperature sintering at 800 °C. XRD analyses showed that the resultant bulk samples exhibit the layered LCO or NMC phases with a low amount of cation intermixing. Moreover, the presence of additional NiO and  $\text{Co}_3\text{O}_4$  phases was detected in NMC with a pronounced nominal Li deficiency of  $x = 0.65$ . As a tracer source, a  $^6\text{Li}$  tracer layer with the same chemical composition was deposited using ion beam sputtering. Secondary ion mass spectrometry in depth profile mode was used for isotopic analysis. The diffusivities followed the Arrhenius law with an activation enthalpy of about 0.8 eV and were nearly identical within error for all samples investigated in the temperature range up to 500 °C. For a diffusion mechanism based on structural Li vacancies, the results indicated that varying the Li content does not result in a change in the vacancy concentration. Consequently, the design and use of a cathode initially made of a Li-deficient material will not improve the kinetics of battery performance. The possible reasons for this unexpected result are discussed.

**Keywords:** Li-ion battery cathode material;  $\text{LiNi}_{1/3}\text{Mn}_{1/3}\text{Co}_{1/3}\text{O}_2$ ;  $\text{LiCoO}_2$ ; Li diffusion; Li off-stoichiometry



Academic Editor: Shaokun Chong

Received: 30 November 2024

Revised: 15 January 2025

Accepted: 18 January 2025

Published: 21 January 2025

**Citation:** Hüger, E.; Uxa, D.; Schmidt, H. Lithium Tracer Diffusion in  $\text{Li}_x\text{CoO}_2$  and  $\text{Li}_x\text{Ni}_{1/3}\text{Mn}_{1/3}\text{Co}_{1/3}\text{O}_2$  ( $x = 1, 0.9, 0.65$ )-Sintered Bulk Cathode Materials for Lithium-Ion Batteries. *Batteries* **2025**, *11*, 40. <https://doi.org/10.3390/batteries11020040>

**Copyright:** © 2025 by the authors. Licensee MDPI, Basel, Switzerland.

This article is an open access article distributed under the terms and conditions of the Creative Commons Attribution (CC BY) license (<https://creativecommons.org/licenses/by/4.0/>).

## 1. Introduction

The diffusion of lithium (Li) in electrode materials [1–11] of rechargeable Li-ion batteries (LIBs) is a determining factor for the incorporation and removal of Li into/from electrodes during electrochemical cycling. Diffusion directly influences charging/discharging times, power densities, maximum capacities, stress development and possible side reactions. In this context, the Li diffusion in electrode materials is of importance for the

optimization of battery performance. Within the class of cathodes,  $\text{LiNi}_y\text{Mn}_z\text{Co}_{1-y-z}\text{O}_2$  ( $y + z < 1$ ) active materials are important for applications and fundamental studies (see references [12–15]). Noteworthy compositions include those with  $y = z = 0$  ( $\text{LiCoO}_2$ , referred to as LCO),  $y = 1, z = 0$  ( $\text{LiNiO}_2$ , referred to as LNO) and  $y = z = 1/3$  ( $\text{LiNi}_{1/3}\text{Mn}_{1/3}\text{Co}_{1/3}\text{O}_2$ , referred to as NMC) [16].

A review of the literature indicates a substantial body of theoretical and computational research focusing on diffusion in cathode materials [17–24]. In contrast, experimental investigations on Li tracer diffusion, including the determination of diffusivities, activation energies, pre-exponential factors and the mechanism of diffusion are relatively limited for these materials. The knowledge on chemical diffusion in cathode materials is predominantly derived from electrochemical measurements such as galvanostatic and potentiostatic intermittent titration techniques (GITT and PITT) and electrochemical impedance spectroscopy (EIS) [5,25–31]. It should be noted that these non-Li selective methods are typically only applicable at, or in the proximity of, room temperature. Consequently, they offer limited insights into activation energies, pre-exponential factors, the underlying defect structure and the diffusion mechanism. Electrochemical measurements of diffusivities are known to be limited by a number of factors, including interfacial processes, parasitic electronic currents, ohmic resistances and side reactions. These factors lead to a substantial variation in diffusivities [21] across different studies and methods, as well as during lithiation/delithiation [5,21].

In contrast, tracer methods provide a direct measurement of the Li tracer diffusivity, eliminating the need for model-dependent correction factors. For a basic introduction into diffusion science, we refer to references [32–35]. Recently, we conducted preliminary research on Li tracer diffusion in sintered bulk samples of NMC with stable isotopes ( $^6\text{Li}/^7\text{Li}$ ) and isotope depth profiling using secondary ion mass spectrometry (SIMS) [2]. Li tracer diffusivities between 110 and 350 °C are temperature dependent and show an activation enthalpy of 0.85 eV. This was interpreted as the migration energy of a single Li vacancy and it was concluded that Li diffusion takes place via structural vacancies, where the concentration is fixed by a low Li deficiency. At room temperature, the Li tracer diffusivity [5] is considerably lower than the chemical diffusivities reported in the literature from electrochemical measurements, which can be attributed to a significant thermodynamic factor correlating both types of diffusivities [5,35]. In a separate publication, it was observed that the NMC and LCO compounds exhibited the same Li diffusivities within error bars [10]. This observation shows that a change in the transition metal (M) within the  $\text{LiMO}_2$  structure does not result in a significant influence on Li tracer diffusion.

Moreover, a comparative study of Li tracer diffusion in LCO single crystals and polycrystalline material was performed [3]. It has been evidenced that the Li diffusivities in the ab-plane of single crystals are the same as those observed in polycrystalline LCO. This finding indicates only a small impact of grain boundaries on the predominant Li-ion migration pathways within the material. Along the c-axis, diffusivities are significantly lower. This experimentally evidenced the often-postulated slow Li diffusion along the c-axis. We suggest that Li diffusion along the c-axis of the 2D ion conductor is controlled by a slow transfer of Li ions between the Li-O layers across the Co-O layers [3].

Recently [36], we reported Li tracer diffusivities in sputter-deposited 1-micrometer-thin amorphous and crystallized NMC films. The diffusivities in crystalline thin films and in sintered bulk materials were found to be nearly identical. In contrast, the Li diffusivities in the amorphous state were found to be lower due to a higher activation enthalpy. The higher activation enthalpy was attributed to hindered Li diffusion in the disordered amorphous state, emphasizing the aspect of disorder for Li diffusion.

In the present study, we investigated Li diffusion in polycrystalline bulk  $\text{Li}_x\text{CoO}_2$  and  $\text{Li}_x\text{Ni}_{1/3}\text{Mn}_{1/3}\text{Co}_{1/3}\text{O}_2$  ( $x = 1, 0.9, 0.65$ ) cathode materials. In order to illustrate the choice of these materials, we would like to mention that LCO and NMC are among the most used materials for positive electrodes of commercial LIBs. Beneath their suitability from a chemical point of view, the active material is typically used in the form of micrometer- or nanometer-sized crystalline particles surrounded by binder and conductive agents to form micrometer-thick polycrystalline layers. These are polycrystalline but consist of single particles bonded together. In order to determine intrinsic Li transport, it is necessary to measure the Li diffusivity in sintered LCO and NMC bulk pellets without additives. High temperature sintering at 800 °C for 24 h was performed to ensure the formation of a crystallographic phase with a layered structure, necessary for the smooth intercalation and deintercalation of Li ions. This will be discussed in detail in the third section.

The aim of the study was to understand the influence of varying the Li content on Li diffusion, which is important for the overall performance of an LIB in two ways.

First, in a recent study on bulk sintered NMC based on SIMS tracer diffusion experiments, we demonstrated that electrochemical delithiation of about 10% charge (Li deficient state) increases the Li tracer diffusivity by orders of magnitude [5]. Moreover, Figure 1 shows Li chemical diffusivities as a function of the working electrode potential,  $E_{we}$ , on the lower  $x$ -axis, and the corresponding Li deficiency, expressed as  $\delta = 1 - x$ , in  $\text{Li}_x\text{Ni}_{1/3}\text{Mn}_{1/3}\text{Co}_{1/3}\text{O}_2$  on the upper  $x$ -axis. The Li deficiency was realized using electrochemical delithiation. The symbols in Figure 1 indicated as “Hüger” are Li chemical diffusivities obtained in our laboratory using PITT and EIS on the same type of sintered NMC pellets ( $x = 1$ ) as used in the current work for SIMS diffusion experiments [5] (see Section 2). The remaining diffusivities on NMC in Figure 1 correspond to values reported by other research groups. As indicated in Figure 1, the data are from Kang et al. [30] (binder- and additive-free films; GITT), Charbonneau et al. [29] (films with NMC particles embedded in binders and conductive additives; EIS) and Wu et al. [26] (films with NMC particles embedded in binders and conductive additives; GITT). These chemical diffusivities also show an increase of several orders of magnitude when significant Li is extracted from the cathode material (around 3.6 V and  $\delta = 1 - x \approx 0.1$ ). Moreover, reference [5] demonstrates that the Li chemical diffusivities are in good agreement with the Li tracer diffusivities obtained from SIMS experiments when the thermodynamic factor is taken into account. Electrochemical investigations [37,38] on Li-deficient  $\text{Li}_x\text{Ni}_{1/3}\text{Mn}_{1/3}\text{Co}_{1/3}\text{O}_2$  ( $x < 1$ ) indicate improved properties as a cathode material.

Such an enhanced Li diffusivity can be advantageous for LIB operation if the NMC electrode shows it already in the initial state right after synthesis. In order to achieve this, the electrode has to be produced with a Li deficiency using appropriate methods like a solid-state reaction. The difference between Li-deficient electrode samples made using a solid-state reaction and electrochemical delithiation has to be elucidated. A possible difference may lie in a high-temperature treatment and the resulting more homogeneous structure of the sample prepared using the solid-state synthesis. The electrochemically obtained delithiations were performed at room temperature, which might result in more Li trapping defects and a higher inhomogeneity due to the presence of two-phase delithiation processes (see e.g., Figure 5 in reference [39] and Figure S4 in reference [5]). Therefore, the solid-state synthesis can be expected to minimize these effects, and this is discussed in detail in the Section 3.

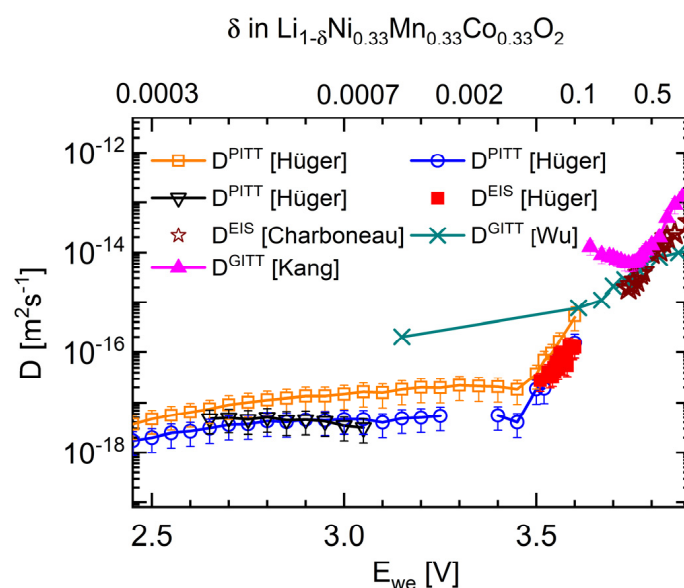


**Figure 1.** Literature data on Li chemical diffusivities as a function of potential ( $E_{we}$ ) and Li deficiency ( $\delta = 1 - x$ ) in  $\text{Li}_x\text{Ni}_{0.33}\text{Mn}_{0.33}\text{Co}_{0.33}\text{O}_2$  as obtained from EIS, PITT and GITT measurements. The data of Hüger correspond to an NMC ( $x = 1.0$ ) sample that was also used for tracer diffusion studies [5]. The other literature data are from Charboneau et al. [29], Kang et al. [30] and Wu et al. [26]. Reference is made to the main text for further description. Reproduced with permission of the authors under their license CC-BY 4.0.

Further, a recent review has identified the critical role of Li off-stoichiometry for the performance of LNO batteries [16]. This may also be relevant for the case of isostructural NMC and LCO. The presence of a slight initial Li deficiency in LNO may result in a reduction in Li diffusivities due to the Ni atoms present in the  $\text{Li}_2\text{O}$  interlayers, which can impede Li diffusion [16]. It is recommended that such electrodes are avoided for optimized LIB cycling. Further discussion on this subject is given in the third section. Accordingly, the latter concept suggests that Li diffusion in initially Li-deficient NMC cathodes may be hindered [16], rather than enhanced as proposed above [5].

It might also be argued that a reduced initial Li content in the cathode material is not beneficial because it reduces the Li content of a full cell, especially for  $x = 0.65$ . A high deficiency can also make the material less stable. This can lead to a lower energy density, shorter cycle life, reduced stability and reduced safety.

The present study exactly evaluates this contradiction in the literature by investigating the Li diffusion properties in polycrystalline bulk  $\text{Li}_x\text{CoO}_2$  and  $\text{Li}_x\text{Ni}_{1/3}\text{Mn}_{1/3}\text{Co}_{1/3}\text{O}_2$  cathode materials with nominally no Li deficiency ( $x \approx 1$ ), medium Li deficiency ( $x \approx 0.9$ ) and even high Li deficiency ( $x \approx 0.65$ ) to examine the effect of Li deficiency on Li tracer diffusion. The current study focuses mainly on the differences between  $x = 0.9$  and  $x = 1.0$ . For a sake of completeness and to address fundamental aspects, we included a strongly off-stoichiometric sample with  $x = 0.65$ . A priori, this sample was not considered as a perspective for LIB operation, but at such a high Li off-stoichiometry, “inactive domains” [40] may appear in NMC during delithiation, which do not re-lithiate and reduce the LIB capacity [16]. Although the present study was not performed during LIB cycling, the investigation of Li diffusion in LCO and NMC cathode materials with Li off-stoichiometry may provide information on the influence of diffusion on the kinetic limitation during re-lithiation.

This paper is structured as follows: After the introductory section, the second section describes the measurement techniques and the preparation of the LCO and NMC materials. The third section starts with a part on structural and chemical sample characterization

(Section 3.1). The analysis is closely linked to literature which should help to understand Li diffusion. The measurement, analysis and discussion of the Li diffusion data are presented in Section 3.2. The final section summarizes the results.

## 2. Experimental Details

The samples were prepared via solid-state synthesis, utilizing a two-step reaction route. Powders of  $\text{Li}_2\text{CO}_3$  were obtained from Sigma Aldrich (Taufkirchen, Germany), while powders of  $\text{NiO}$ ,  $\text{MnO}_2$  and  $\text{Co}_3\text{O}_4$  were obtained from Carl Roth (Karlsruhe, Germany). The powder materials were introduced into an agate ball milling tank (WiseMix Ball Mill, Wisd Laboratory Instruments, Wertheim, Germany) with respect to the required Li to metal ratio and with the addition of an appropriate amount of ethanol as a dispersing agent. The mixture was subjected to a ball-milling process at a rate of 150 rpm (rotations per minute) for a duration of 1 h. Afterwards, the dried powder mixture was subjected to a thermal treatment at 800 °C (16 h) at a rate of 3 K/min in pure oxygen. The powder mixture thus obtained was subjected to high-energy ball milling (SPEX 8000M shaker mill, SPEX, CertiPrep, SampleSpec, Metuchen, NJ, USA) for a total of 4 min at 1080 cycles per minute with zirconia ceramic balls, and a pellet was subsequently pressed at 100 MPa and sintered at 800 °C in air for a long period of 24 h. This process resulted in polycrystalline, dense samples with relative densities of approximately 97% [2]. The thickness of the LCO and NMC pellets was approximately 1 mm and the diameter was about 8 mm. For two types of samples (LCO,  $x = 1.0$  and NMC,  $x = 0.9$ ), a modified procedure was applied. LCO and NMC powders were bought from Alfa Aesar (Kandel, Germany) and Sigma-Aldrich (Taufkirchen, Germany), respectively. Afterwards, the high energy milling and pressing steps were carried out accordingly.

The relative Li concentration was determined by analyzing the samples using inductively coupled plasma-optical emission spectroscopy (ICP-OES) with a Plasma Quant 9100 machine (Analytik Jena, Jena, Germany). By varying the initial  $\text{Li}_2\text{CO}_3$  fraction, we obtained  $\text{Li}_x\text{CoO}_2$  and  $\text{Li}_x\text{Ni}_{1/3}\text{Mn}_{1/3}\text{Co}_{1/3}\text{O}_2$  samples with nominal Li amounts of approximately 1.0, 0.9 and 0.65.

The sputter targets for tracer layer deposition were produced in an analogous manner using isotope-enriched  $^6\text{Li}_2\text{CO}_3$  (95% enriched) as the starting material instead. Due to the larger diameter of the sputter target (about 20 mm), a higher pressure of 330 MPa was applied. The deposition of the tracer was achieved with the help of ion-beam coating, performed with a commercially available apparatus (IBC 681, Gatan, Irvine, CA, USA). The thicknesses of the tracer layers were between 70 and 110 nm. The deposition was carried out at an energy of 5 keV and a current of 200  $\mu\text{A}$  with argon sputter gas at  $5 \times 10^{-3}$  mbar. Given that the  $^6\text{Li}$  tracer layer and the bulk sample have a similar chemical composition (resulting from the same production route), it was anticipated that pure isotope interdiffusion would occur during the diffusion experiments. The sputtered samples were annealed at elevated temperatures in air using a commercial rapid annealing setup (AO 600, MBE Komponenten, Weil der Stadt, Germany). The structural investigation of the bulk samples was carried out using X-ray Diffractometry (XRD) on a Bruker D8 Discover diffractometer (Bruker AXS Advanced X-ray Solutions GmbH, Karlsruhe, Germany) in  $\theta/2\theta$  mode with  $\text{CuK}_\alpha$  radiation at 40 keV and 40 mA.

Depth profiles of the two Li isotopes and of the Ni, Mn and Co species were recorded using SIMS. For this investigation, a Cameca IMS 3f/4f machine (CAMECA SAS, Gennevilliers Cedex, France) with  $\text{O}^-$  primary ions was applied. SIMS was used in depth profile mode. A beam of  $\text{O}^-$  primary ions was directed onto the sample and scanned over the surface in an area of approximately  $250 \mu\text{m} \times 250 \mu\text{m}$  to sputter away material, creating a zone with a crater-like depression termed “sputter crater”. This crater was measured

with a mechanical stylus profilometer (Tencor Alphastep 500, Milpitas, CA, USA) for depth calibration. The relative  ${}^6\text{Li}$  isotope fraction,  $c$ , was calculated from the  ${}^6\text{Li}$  and  ${}^7\text{Li}$  signal intensities,  $I$ , as measured using SIMS.

$$c = \frac{I({}^6\text{Li})}{I({}^6\text{Li}) + I({}^7\text{Li})} \quad (1)$$

### 3. Results and Discussion

#### 3.1. Structural Characterization and Relative Li Concentration

Before presenting the diffusion results, which is the main task of the current study, we present investigations on the structure and chemical composition of the LCO and NMC samples and discuss the expected effects on Li diffusion.

For the determination of the relative Li concentration, the samples were analyzed using ICP-OES and the results are shown in Table 1. By varying the initial  $\text{Li}_2\text{CO}_3$  fraction, we obtained  $\text{Li}_x\text{CoO}_2$  and  $\text{Li}_x\text{Ni}_{1/3}\text{Mn}_{1/3}\text{Co}_{1/3}\text{O}_2$  samples with nominal Li amounts of approximately  $x = 1.0, 0.9$  and  $0.65$ , where  $x$  corresponds to the Li to metal ratio  $L/M$ .

**Table 1.** Relative metal element concentrations as analyzed using ICP-OES of the samples under investigation.  $L/M$  denotes the Li to metal ratio.

Sample	Li (at.%)	Ni (at.%)	Mn (at.%)	Co (at.%)	$L/M$
LCO ( $x = 1$ )	$24.64 \pm 0.13$	--	--	$24.94 \pm 0.21$	$0.99 \pm 0.01$
LCO ( $x = 0.9$ )	$22.72 \pm 0.02$	--	--	$25.08 \pm 0.17$	$0.91 \pm 0.01$
NMC ( $x = 1$ )	$24.09 \pm 0.10$	$7.72 \pm 0.03$	$7.82 \pm 0.01$	$8.32 \pm 0.04$	$1.01 \pm 0.01$
NMC ( $x = 0.9$ )	$22.50 \pm 0.10$	$7.42 \pm 0.02$	$9.88 \pm 0.06$	$8.05 \pm 0.04$	$0.89 \pm 0.01$
NMC ( $x = 0.65$ )	$18.20 \pm 0.10$	$9.66 \pm 0.13$	$9.29 \pm 0.14$	$8.92 \pm 0.16$	$0.65 \pm 0.01$

X-ray diffraction patterns of the sintered sample are shown in Figure 2a. Most of the Bragg peaks correspond to the rhombohedral (or hexagonal)  $\alpha\text{-NaFeO}_2$ -type layered structure belonging to the  $R\text{-}3m$  space group (see indexing). The results show that LCO and NMC samples with  $x = 1$  and  $0.9$  show no obvious impurity phases. This indicates an upper limit of possible impurity phases of 3–5% corresponding to the detection limit. For the NMC sample with  $x = 0.65$ , additionally, amounts of  $\text{NiO}$  and  $\text{Co}_3\text{O}_4$  phases in the ten percent range can be detected due to the strongly reduced Li content. The exact amount of impurity phases was not of importance for this diffusion study, as long as no percolation path was formed, which is the case.

Beneath the detected hexagonal high temperature structure, low-temperature spinel (cubic,  $Fd3m$ ), and rock-salt (cubic, random occupation of the cation sites) phases have been reported for LCO and NMC [11,16,39,41–64]. Note that the difference in the XRD patterns between the hexagonal phase and the spinel phase is very small [42]. The main indication is a slightly different  $2\theta$  position of the strongest reflection, (003) for the layered and (111) for the spinel phase, a splitting of the spinel reflection (222) into the layered (006) and (012) reflections, and the splitting of the spinel (440) reflection into the layered (018) and (110) reflections [39,44].

For  $\text{Cu K}\alpha$  radiation and LCO, the layered (003) reflection was located at  $2\theta = 18.94^\circ$  and the spinel (111) reflection was located at  $2\theta = 19.17^\circ$  [44]. The measured XRD patterns of the current study with  $x = 1$  and  $0.9$  in  $\text{Li}_x\text{CoO}_2$  show only a single strong reflection located at  $2\theta = 18.9^\circ$  and no reflection at  $2\theta = 19.2^\circ$  (see Figure 2b). The reflection splitting of (006), (012), (018) and (110) was also well-resolved in the measurement (see Figure 2c,d). This indicates that the LCO pellets consist of the layered hexagonal phase only, which can

be expected due the sintering for 24 h at the high temperature of 800 °C. Cho et al. [38] have shown that the phase transition of NMC to its layered phase only occurs after the lithium carbonate ( $\text{Li}_2\text{CO}_3$ ) has fully reacted at a temperature above 660 °C. Figure 2 shows no evidence of  $\text{Li}_2\text{CO}_3$ , which is also expected for LCO only for  $x \geq 1$ , as reported in the literature [42]. An excess of Li is commonly aimed to minimize off-stoichiometry and to compensate for the loss of Li during the calcination process [16]. However, the presence of the cubic phases in very small amounts below the detection limits of XRD cannot be excluded, but they are not expected to form a percolation path and will not influence Li diffusion.

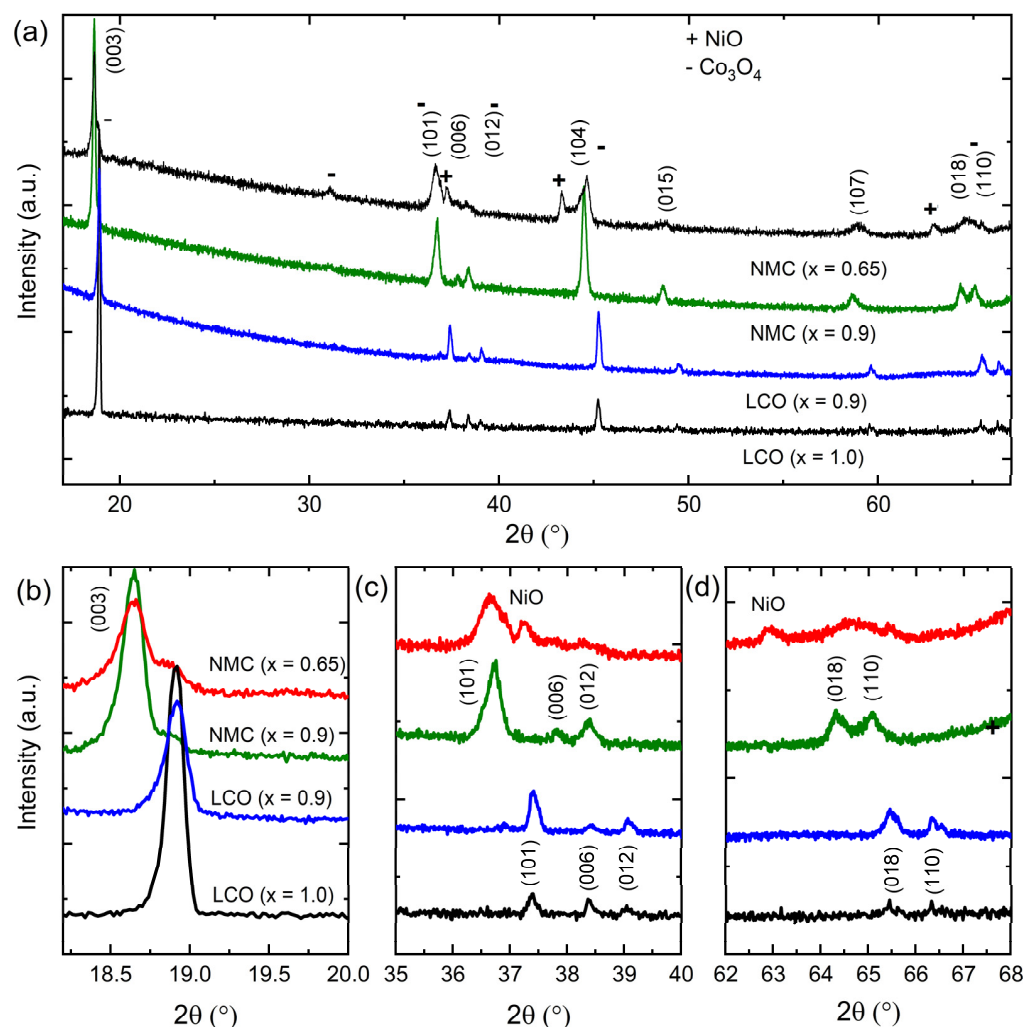


**Figure 2.** X-ray diffraction patterns of bulk NMC and LCO samples under investigation. Bragg peaks corresponding to the main NMC or LCO phase are indexed (hexagonal scheme) and impurity phases are marked: (a) overview and (b–d) enlarged views.

For further discussion, note that the hexagonal phase has a structure of Li layers alternating with transition metal (e.g., Co) layers between oxygen layers. LCO and NMC both obey this layered structure type, but show a subtle difference. The Ni and Mn content in NMC more often leads to the mixing of Li and Ni cations on the different sub-lattices as anti-site defects also termed cation mixing, which occurs both during synthesis and cycling. This means that the transition metal is located in the Li layer, replacing a Li ion there, and that Li is located in the transition metal oxide. This type of defect may have a strong influence on Li diffusion [16,57]. A high cation mixing rate in the cathode materials is expected to give a lower Li diffusivity and a higher activation enthalpy [49]. Li/transition

metal anti-site defect disorder also directly correlates to the electrochemical properties [59]. The most homogeneous samples have the highest capacity, lowest voltage polarization, lowest capacity fade and highest initial coulombic efficiency [59]. The Li/transition metal exchange was visualized using TEM [39,54,55,57]. For LCO, this effect is expected to only be small [45,47,49,51,52,56,57].

XRD studies developed two simple criteria that may indicate cation mixing in the layered phase. If the integrated intensity ratio  $I(003)/I(104) < 1.2$  and the positions of the (018)/(110) pairs of reflections begin to merge, then transition metal (e.g., Ni) and Li ion mixing is very likely occurring [39,53]. Here,  $I(003)/I(104) \approx 6.6$  was high for LCO and  $x = 1$ , indicating nearly no Co/Li ion mixing. The integrated intensity of  $I(003)/I(104) \approx 2$  for  $x = 0.9$  was still above the threshold of 1.2, indicating a low mixing rate, but slightly more Li/Co antisite defects. Calculations [52,56] predict an anti-site defect concentration of only 0.002% in LCO at 1000 K. The introduction of Mn and Ni for NMC should cause an increase in the anti-site defect concentration [52], which is highest for LNO at up to almost 13%. A recent review on why anti-site defects occur can be found in [57]. Attempts have been made to reduce the amount of anti-site defects using surface engineering (deposition of surface layers) and/or volume engineering by doping NMC with other transition metals to stabilize the transition metal–oxygen skeleton [11,16,57,60,62,63].

In the case of NMC ( $x = 0.9$ ) (Figure 2), the (003) hexagonal reflection is located at  $2\theta = 18.7^\circ$ , which corresponds to the value reported in the literature [50]. There is also a small reflection at  $2\theta = 18.9^\circ$ , which could be from LCO, but is more likely from a spinel phase.  $\text{Co}_3\text{O}_4$  can also not be excluded, but is unlikely, since no other higher intensity peaks of that phase occur here. However, the position of the layered (006), (012), (018) and (110) reflections is also well-resolved in the measurement. The ratio of the integrated intensity of  $I_{(003)}/I_{(104)} \approx 1.3$  for NMC with  $x = 0.9$  was close to the threshold of 1.2. These results show that the NMC sample had a layered hexagonal phase with, as expected, a higher, but still low, concentration of cation mixing.

For a high Li deficiency ( $x = 0.65$ ), beneath the already mentioned impurity phases, the XRD pattern showed a ratio of  $I_{(003)}/I_{(104)} \approx 1.6$ , which was again close to threshold of 1.2. The (006), (012), (018) and (110) reflections of the layered phase can also be assumed to exist separately, but were not well-resolved. Therefore, we assume that this sample also shows the layered hexagonal phase together with the NiO- and  $\text{Co}_3\text{O}_4$ -impurity phases.

The Li/transition metal mixing is expected to be strongly reduced through a long heating time (more than 5 h) at temperatures as high as  $800^\circ\text{C}$  [48,53], as was performed in this study. However, diffraction experiments on NMC [45] found that, even after annealing at  $900^\circ\text{C}$ , a small proportion ( $\approx 2\%$ ) of the Ni may be located at the Li site, displacing an equal amount of Li to the transition metal site, in agreement with our findings.

A strategy to reduce the number of anti-site defects is the preparation of Li-rich samples. However, experimental work on optimizing the NMC electrode material by adjusting the Li/transition metal ratio always resulted in the presence of a low amount of anti-site defects, where  $\approx 2\%$  seems to be a threshold [47]. A Li deficiency is expected to first produce Li/transition metal anti-site defects [16,41,43]), followed by the appearance of the rock salt phase for a higher Li deficiency (see, e.g., Figure 1 in reference [54]). As recently discussed for LNO [16], due to the ability of Ni to induce cation mixing, this material tends to be under-stoichiometric in Li and contains excess  $\text{Ni}^{2+}$  located in the Li layers, which strongly affects its physicochemical properties [16]. The synthesis of LNO samples yields compounds that always contain 0.99–0.98 in  $\text{Li}_x\text{NiO}_2$  even under very well-controlled conditions [16].

With regard to other point defects, it is worth mentioning that oxygen vacancies are thought to promote a proper atomic rearrangement and a more defect-free layered phase

using diffusion during annealing at high temperatures. LCO films deposited using laser ablation at low oxygen pressures produce oxygen vacancies that enhance cation mobility and favor the hexagonal phase [44]. A high-temperature treatment is necessary to allow the transition metal (e.g., Ni) to diffuse from the Li/Ni anti-site position to the regular position. The role of oxygen vacancies also plays a role in the reverse case, i.e., in the conversion of the layered phase into other phases, e.g., into the spinel phase [65], during electrochemical Li extraction. There, the transition metal ions must diffuse from the transition metal layer into the Li layer [65]. This has to occur by squeezing the transition metal through a densely packed oxygen layer. This process would be accelerated due to the presence of oxygen vacancies. Furthermore, oxygen vacancies in cathode materials can also play a beneficial role for LIB cycling of Li-rich NMC cathode materials [16,66–68]. It has been found that oxygen depletion of the surface layer is one way to improve the cyclability of this family of cathode materials [16,66–68]. Theoretical calculations and experimental characterizations show that oxygen vacancies provide a favorable environment for ionic diffusion in the bulk and significantly suppress oxygen gas release from the surface [68]. These facts indicate that not only the knowledge of Li diffusion is important for NMC materials, but also the diffusion of oxygen and transition metals.

In summary, the long annealing time at 800 °C of the LCO and NMC samples resulted in a hexagonal layered phase with a low number of Li/transition metal anti-site defects. NMC with  $x = 0.65$  showed additional NiO and  $\text{Co}_3\text{O}_4$  impurity phases, also as expected from the results published in the literature [42]. Impurity phases (including the spinel phase) are not expected to form a percolation path and will not affect Li diffusion. XRD suggested that the number of anti-site defects and, consequently, the Li diffusion should decrease from LCO with  $x = 1$  to LCO with  $x = 0.9$ , to NMC with  $x = 1$ , to NMC with  $x = 0.9$  and to NMC with  $x = 0.65$ . This trend is in contrast to the electrochemical delithiation experiments in Figure 1, which show the opposite behavior. The Li tracer diffusivity measurements of the following section should give more insights in this regard.

### 3.2. Li Tracer Diffusion Measurements

Figure 3 provides an illustration of typical SIMS depth profiles (relative  $^6\text{Li}$  fraction vs. depth) observed after tracer deposition and diffusion annealing at elevated temperatures for a specified time for each sample type. For further examples of typical depth profiles, we refer to references [2,10].

After tracer deposition, we obtained a well-localized  $^6\text{Li}$  distribution, restricted to the first 100 nm of the depth profile superimposed on the natural  $^6\text{Li}$  background of the sample. This corresponds to the as-deposited tracer layer. After annealing, we noted a clear penetration of the  $^6\text{Li}$  tracer deep into the sample. This redistribution of  $^6\text{Li}$  was caused by isotope diffusion and can be used to determine the Li tracer diffusivity by comparing the experimental data to appropriate solutions of Fick's second law.

Without diffusion annealing, the depth profile may be fitted with the thick-film solution of Fick's second law [69] as follows:

$$c(x,t) = c_\infty + \frac{(c_0 - c_\infty)}{2} \left[ \operatorname{erf}\left(\frac{h+x}{R}\right) + \operatorname{erf}\left(\frac{h-x}{R}\right) \right]. \quad (2)$$

In Equation (2),  $c_\infty$  is defined as the residual  $^6\text{Li}$  isotope fraction in the NMC or LCO bulk sample, while  $c_0$  signifies the  $^6\text{Li}$  fraction present in the  $^6\text{Li}$ -enriched layer. The thickness of the  $^6\text{Li}$ -enriched layer is denoted as  $h$ , and  $R = R_0$  is the broadening of the Li distribution at the interface. The diffusion process of the  $^6\text{Li}$  tracer into the specimen, initiated during the annealing procedure, results in the broadening of the  $^6\text{Li}$  distribution, denoted by  $R$ . To determine the Li tracer diffusivities, the profiles of diffusion-annealed

specimens were also fitted with Equation (2). In this context,  $R$  serves as a fit parameter, while the value of  $h$  is fixed to its initial value. The Li diffusivity ( $D$ ) is thus determined from the difference in the respective broadening of the  ${}^6\text{Li}$  distribution of the annealed profile ( $R$ ) and of the as-deposited profile ( $R_0$ ). This is expressed as follows:  $D = (R^2 - R_0^2)/4t$ , where  $t$  is the annealing time. The results of the fitting process are displayed as continuous red lines in Figure 3.

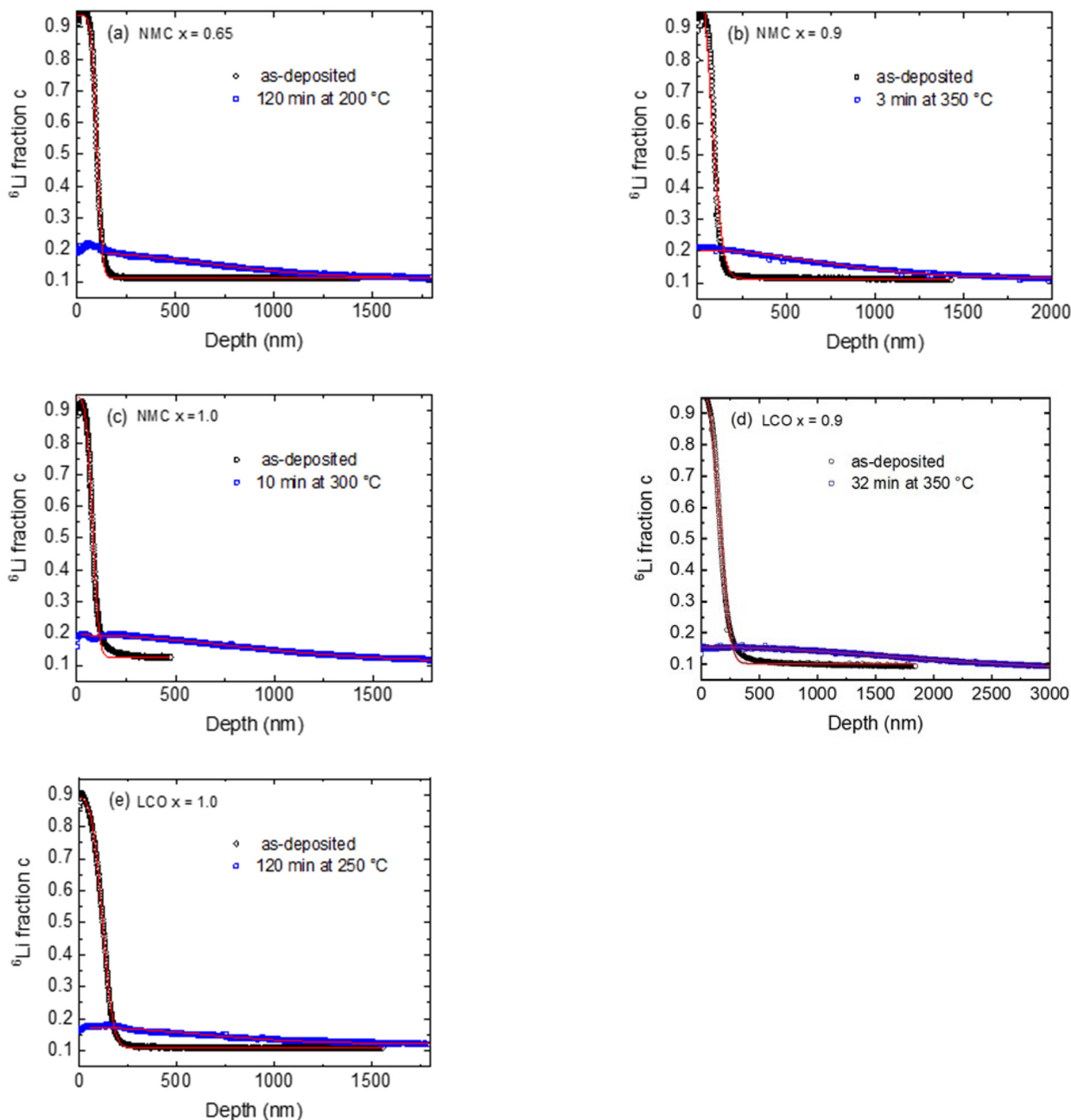


**Figure 3.**  ${}^6\text{Li}$  fraction,  $c$ , as a function of depth for various types of samples directly after tracer deposition and after annealing of (a) NMC with  $x = 0.65$ , (b) NMC with  $x = 0.9$ , (c) NMC with  $x = 1.0$ , (d) LCO with  $x = 0.9$ , and (e) LCO with  $x = 1.0$ . The fit of curves according to Equation (2) is plotted with red continuous lines.

In Figure 4, all Li tracer diffusivities determined are depicted as a function of the reciprocal temperature. Evidently, the Li diffusivities of all samples are in agreement with each other within error limits, despite statistical deviations. This result clearly demonstrates that the Li diffusivities are independent of the Li fraction between  $x = 1$  and  $0.65$

for the present LCO and NMC samples, which is in contradiction to the expectations of Sections 1 and 3.1.

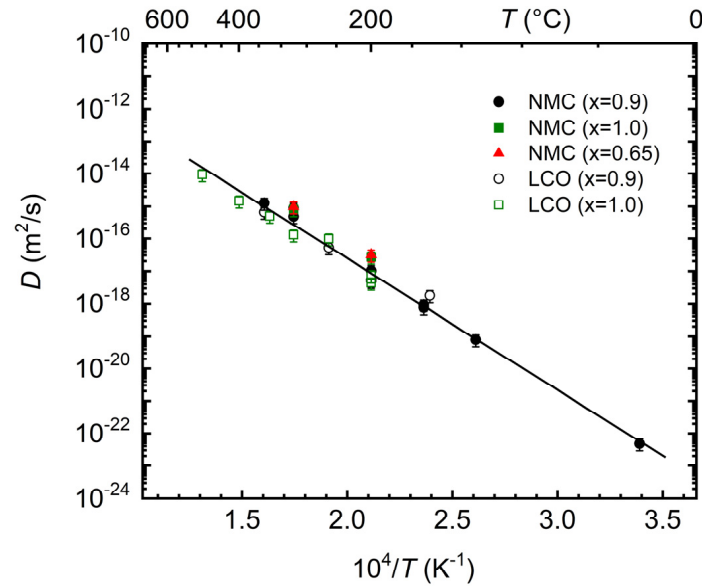


**Figure 4.** Li tracer diffusivities of  $\text{Li}_x\text{CoO}_2$  (LCO) and  $\text{Li}_x\text{Ni}_{1/3}\text{Mn}_{1/3}\text{Co}_{1/3}\text{O}_2$  (NMC) as a function of reciprocal temperature for different values of  $x$ , as measured using SIMS.

The diffusivities follow the Arrhenius law:

$$D = D_0 \cdot \exp(-\Delta H/kT) \quad (3)$$

where  $\Delta H$  is the activation enthalpy of diffusion and  $D_0$  is the pre-exponential factor. A least-squares fit of Equation (3) to the diffusivities gives an activation enthalpy of  $\Delta H = (0.80 \pm 0.03)$  eV and a pre-exponential factor of  $D_0 = 3.1_{-1.5}^{+2.9} \times 10^{-9}$  m<sup>2</sup>/s, where preliminary data were published in references [2,3,5,10].

Following the arguments of ref. [2], it was hypothesized that all samples under investigation were at least slightly Li sub-stoichiometric, including the samples considered to be nominally  $x \approx 1$ . This sub-stoichiometry can be attributed to the presence of structural vacancies in the Li sub-lattice. Consequently, the calculated activation enthalpy of diffusion is equivalent to the migration enthalpy of diffusion of the Li ions,  $\Delta H = \Delta H_m \approx 0.8$  eV. In comparison to the results of first principles calculations employing the pseudopotential method within the local density approximation of density functional theory, a monovacancy mechanism can be postulated based on a direct next-neighbor hop of a Li-ion into a Li vacancy. Migration enthalpies of 0.8 eV [70] and 0.7 eV [71] were calculated, which is in good agreement with the measured activation enthalpy.

For structural Li vacancies, the pre-exponential factor is given by

$$D_0 = f_V a^2 \nu_0 \exp\left(\frac{\Delta S_m}{k_B}\right) \quad (4)$$

neglecting the correlation factor. In this context, it is important to note that  $a = 0.286$  nm names the shortest Li-Li atomic distance, while  $\nu_0$  is approximately equal to  $1 \times 10^{13}$  s<sup>-1</sup> and is a characteristic vibration frequency. Furthermore,  $f_V$  denotes the fraction of structural vacancies, while  $\Delta S_m$  is approximately equal to 0–1 k<sub>B</sub> and denotes the migration component of the entropy of diffusion. The application of Equation (4) to the experimentally determined pre-exponential factor enables the assessment of a mole fraction of vacancies within the range of  $f_V = 10^{-2} - 10^{-3}$ .

This low  $f_V$  value obtained for all samples investigated means that the mole fraction of vacancies was not correlated to the fraction of Li ions present in the samples. For example, for  $x = 0.65$ , a fraction of vacancies of  $f_V = 1 - x = 0.35$  would be expected, if it is assumed that each one lacking Li results in a vacancy. Consequently, it can be assumed that during sample synthesis with the solid-state reaction route, as was performed in this study, the same number of structural vacancies is always formed within the material. The vacancy concentration corresponds to the border of the stability range of the sub-stoichiometric NMC phase. Removing more Li will lead to the formation of impurity phases like NiO and  $\text{Co}_3\text{O}_4$ , as detected for the sample with a nominal composition of  $x = 0.65$ .

These results are in contrast to the aspects outlined in the Introduction section, that is, that the removal of Li from the cathode material (Li deficient material) should lead to a strong increase in Li diffusivities/ion conductivities and, consequently, vacancies. This indicates that the vacancy-rich structural state with enhanced diffusion formed during electrochemical delithiation cannot be achieved using a sample synthesis with solid-state reactions.

A second aspect is that the possible presence of cation mixing is expected to block Li diffusion pathways. According to the discussion in Section 3.1, cation mixing and consequently diffusion should decrease with a growing Li deficiency and for NMC compared to LCO. This was also not observed in the results of the SIMS experiments. Consequently, a possible increase in the amount of cation mixing with off-stoichiometry present in the samples is not sufficient to influence diffusion to a measurable extent. However, a blocking of diffusion can already be present for  $x \approx 1$  (nominal), where a small amount of transition metal might be present in the Li interlayer. As mentioned for LNO [16], the synthesis of real electrode samples will result in compounds with  $x \approx 0.99$ , and at least 1% of residual Ni is located in the Li layer even under very well-controlled synthesis conditions. A reduction in  $x$  will not influence Li tracer diffusion any more.

If Li diffusion in LCO and NMC would be predominantly determined based on the degree of cation mixing, then it can be argued that the higher Li diffusivity found at the onset of electrochemical delithiation (Figure 1) is due to a reduction in cation mixing in the Li layers. This is curious, because during delithiation Li is extracted from the Li layers, which would cause the transition metal (i.e., Ni) to jump into the Li layers, increasing rather than decreasing the concentration of anti-site defects.

As mentioned, the decrease in charge capacity during re-lithiation can be described in terms of the formation of 'inactive domains' [16]. Based on the results of the present study, it can be assumed that NMC material is composed of two kinds of domains: active domains that show fast Li diffusion in unblocked Li interlayers (and a reversible Li charge capacity) and inactive domains that show slow diffusion in blocked interlayers. A variation in  $x$  may change the number of these domains. Since the diffusivity does not depend on the Li off-stoichiometry, the electrode with  $x \approx 0.65$  should have percolation paths composed of active domains. This insight, obtained exclusively from Li tracer diffusion experiments, is in agreement with the XRD measurements discussed in Section 3.1 (Figure 2). The XRD analysis indicated the presence of the layered hexagonal crystallographic phase with a low concentration of cation mixing in all electrodes studied, even in NMC with  $x = 0.65$ . The lower Li content only led to the detection of Li-free  $\text{Co}_3\text{O}_4$  and NiO phases. The diffusion experiments showed that these impurity phases do not block the total Li diffusion. Although the impurity phases may have low Li diffusivities, the Li diffusion is not completely blocked because the well-ordered layered phase may still form percolation regions for Li diffusion, even at a Li deficiency corresponding to  $x = 0.65$ . It is briefly mentioned that slow diffusion in the inactive regions has an impact on the re-lithiation

of the NMC [16]. Slow diffusion requires long time intervals for Li to diffuse across the inactive domains, which is typically achieved using constant voltage steps during cycling.

The advantage of the solid-state reaction method with heating at high temperatures may lie in the production of more extended ordered Li layers with a lower degree of cation mixing. The higher the Li deficiency, the higher the proportion of impurity phases. The layered phase creates a percolation path for Li diffusion and thus determines the measured Li tracer diffusivity similar for all the Li-deficient samples.

In this context, it should be mentioned that another, obviously more direct explanation for the results of the SIMS experiments is that thermal annealing of the diffusion samples at temperatures of only 150 °C and above destroy a vacancy-rich state, which will be investigated in the future by annealing electrochemically delithiated samples.

Another aspect is that it is known that even a small removal of Li from LCO and NMC enhances the electronic conductivity and the corresponding activation energy is reduced [30]. At room temperature, the electronic conductivity in NMC increases by more than two orders of magnitude when 10% of Li is electrochemically removed [25]. An explanation for this might be that the sluggish kinetics at the stoichiometric composition ( $x = 1.0$ ) of NMC in the electrochemical cell are charge transfer limited [30]. Based on our results, this was not the case for the present samples, whose Li deficiency was produced using solid-state synthesis and high-temperature annealing.

Nevertheless, the cycling of LCO and NMC not to full Li content may remain a suitable strategy for better LIB cycling from the point of view of Li kinetics.

#### 4. Conclusions

According to the literature, Li diffusivities in the cathode material  $\text{Li}(\text{Ni},\text{Mn},\text{Co})\text{O}_2$  are initially low but increase by orders of magnitude by reducing the Li content during electrochemical LIB operation (delithiation). Such an increase in Li diffusivity will be advantageous for LIB operation if the electrode already shows this enhanced diffusivity in the initial state right after synthesis. Consequently, we produced  $\text{Li}_x\text{CoO}_2$  and  $\text{Li}_x\text{Ni}_{1/3}\text{Mn}_{01/3}\text{Co}_{1/3}\text{O}_2$  cathode materials with different Li fractions of  $x = 1, 0.9$  and  $0.65$  using a solid-state reaction, and carried out Li tracer diffusion experiments in order to understand the influence of varying the Li content on Li diffusion. The measurements were performed on polycrystalline sintered bulk materials, free of additives and binders in order to probe intrinsic properties.

The variation of the Li content  $x$  was achieved through a reactive solid-state synthesis using defined amounts of  $\text{Li}_2\text{CO}_3$ ,  $\text{NiO}$ ,  $\text{Co}_3\text{O}_4$  and/or  $\text{MnO}_2$  powders. LCO and NMC pellets were sintered at 800 °C for 24 h. The resulting samples exhibited the layered hexagonal phase with only low cation intermixing. Unreacted phases of  $\text{NiO}$  and  $\text{Co}_3\text{O}_4$  were detected in NMC, with the most pronounced Li deficiency of  $x = 0.65$ .

The diffusivities followed the Arrhenius law, with an activation enthalpy of about 0.8 eV, and were nearly identical within error limits for all samples investigated in the temperature range up to 500 °C. Nominally Li-deficient cathode materials prepared using the solid-state route did not show a modification in Li diffusion compared to the near-stoichiometric case. If a diffusion mechanism based on structural Li vacancies was operating, the results show that Li deficiency does not result in a modification to the vacancy concentration. This indicates that the vacancy-rich structural state obtained during electrochemical delithiation cannot be achieved using a synthesis with thermally induced solid-state reactions. This is in strong contrast to what happens during electrochemical delithiation, where diffusion is accelerated through a Li-deficient state formed through Li removal from the electrode [5]. Consequently, the design and use of a cathode initially made of a Li-deficient material will not improve the kinetics of battery performance.

**Author Contributions:** Conceptualization, H.S. and E.H.; methodology, H.S. and D.U.; validation, H.S., D.U. and E.H.; formal analysis, H.S., D.U. and E.H.; investigation, D.U. and E.H.; resources, H.S.; data curation, H.S. and E.H.; writing—original draft preparation, H.S. and E.H.; writing—review and editing, H.S. and E.H.; visualization, H.S. and E.H.; supervision, H.S.; project administration, H.S.; funding acquisition, H.S. All authors have read and agreed to the published version of the manuscript.

**Funding:** This research was funded by the Deutsche Forschungsgemeinschaft (DFG, German Research Foundation) under contract SCHM 1569/33-2 (413672097). The financial support is gratefully acknowledged.

**Data Availability Statement:** Dataset available on request from the authors.

**Acknowledgments:** We are indebted to G. Zander for ICP-OES analysis and R. Deichmann for producing the sputter targets.

**Conflicts of Interest:** The authors declare no conflicts of interest.

## References

1. Strauß, F.; Hüger, E.; Julin, J.; Munnik, F.; Schmidt, H. Lithium Diffusion in Ion-Beam Sputter-Deposited Lithium–Silicon Layers. *J. Phys. Chem. C* **2020**, *124*, 8616–8623. [[CrossRef](#)]
2. Uxa, D.; Holmes, H.J.; Meyer, K.; Dörrer, L.; Schmidt, H. Lithium tracer diffusion in  $\text{LiNi}_{0.33}\text{Mn}_{0.33}\text{Co}_{0.33}\text{O}_2$  cathode material for lithium-ion batteries. *Phys. Chem. Chem. Phys.* **2021**, *23*, 5992–5998. [[CrossRef](#)]
3. Uxa, D.; Hüger, E.; Meyer, K.; Dörrer, L.; Schmidt, H. Lithium-Ion Diffusion in Near-Stoichiometric Polycrystalline and Monocrystalline  $\text{LiCoO}_2$ . *Chem. Mater.* **2023**, *35*, 3307–3315. [[CrossRef](#)]
4. Uxa, D.; Schmidt, H. Lithium tracer diffusion in near stoichiometric  $\text{LiNi}_{0.5}\text{Mn}_{1.5}\text{O}_4$  cathode material for lithium-ion batteries. *Z. Für Phys. Chem.* **2022**, *236*, 979–989. [[CrossRef](#)]
5. Hüger, E.; Uxa, D.; Schmidt, H. Electrochemical (PITT, EIS) and Analytical (SIMS) Determination of Li Diffusivities at the Onset of Charging  $\text{LiNi}_{0.33}\text{Mn}_{0.33}\text{Co}_{0.33}\text{O}_2$  Electrodes. *J. Phys. Chem. C* **2024**, *128*, 7408–7423. [[CrossRef](#)]
6. Hasegawa, G.; Kuwata, N.; Tanaka, Y.; Miyazaki, T.; Ishigaki, N.; Takada, K.; Kawamura, J. Tracer diffusion coefficients of Li<sup>+</sup> ions in c-axis oriented  $\text{Li}_x\text{CoO}_2$  thin films measured by secondary ion mass spectrometry. *Phys. Chem. Chem. Phys.* **2021**, *23*, 2438–2448. [[CrossRef](#)]
7. Kuwata, N.; Hasegawa, G.; Maeda, D.; Ishigaki, N.; Miyazaki, T.; Kawamura, J. Tracer Diffusion Coefficients of Li Ions in  $\text{Li}_x\text{Mn}_2\text{O}_4$  Thin Films Observed by Isotope Exchange Secondary Ion Mass Spectrometry. *J. Phys. Chem. C* **2020**, *124*, 22981–22992. [[CrossRef](#)]
8. Schwab, C.; Höweling, A.; Windmüller, A.; Gonzalez-Julian, J.; Möller, S.; Binder, J.R.; Uhlenbruck, S.; Guillon, O.; Martin, M. Bulk and grain boundary Li-diffusion in dense  $\text{LiMn}_2\text{O}_4$  pellets by means of isotope exchange and ToF-SIMS analysis. *Phys. Chem. Chem. Phys.* **2019**, *21*, 26066–26076. [[CrossRef](#)]
9. Takai, S.; Yoshioka, K.; Iikura, H.; Matsubayashi, M.; Yao, T.; Esaka, T. Tracer diffusion coefficients of lithium ion in  $\text{LiMn}_2\text{O}_4$  measured by neutron radiography. *Solid State Ion.* **2014**, *256*, 93–96. [[CrossRef](#)]
10. Uxa, D.; Holmes, H.J.; Meyer, K.; Dörrer, L.; Schmidt, H. Lithium Tracer Diffusion in Sub-Stoichiometric Layered Lithium-Metal-Oxide Compounds. *DDF* **2021**, *413*, 125–135. [[CrossRef](#)]
11. Hüger, E.; Riedel, L.; Zhu, J.; Stahn, J.; Heitjans, P.; Schmidt, H. Lithium niobate for fast cycling in Li-ion batteries: Review and new experimental data. *Batteries* **2023**, *9*, 244. [[CrossRef](#)]
12. Li, Z.; Chernova, N.; Roppolo, M.; Upreti, S.; Petersburg, C.; Alamgir, F.; Whittingham, M. Comparative Study of the Capacity and Rate Capability of  $\text{LiNi}_y\text{Mn}_y\text{Co}_{1-2y}\text{O}_2$  ( $y = 0.5, 0.45, 0.4, 0.33$ ). *J. Electrochem. Soc.* **2011**, *158*, A516. [[CrossRef](#)]
13. Kim, M.-H.; Shin, H.-S.; Shin, D.; Sun, Y.-K. Synthesis and electrochemical properties of  $\text{Li}[\text{Ni}_{0.8}\text{Co}_{0.1}\text{Mn}_{0.1}]\text{O}_2$  and  $\text{Li}[\text{Ni}_{0.8}\text{Co}_{0.2}]\text{O}_2$  via co-precipitation. *J. Power Sources* **2006**, *159*, 1328–1333. [[CrossRef](#)]
14. Wu, F.; Wang, M.; Su, Y.; Bao, L.; Chen, S. Surface of  $\text{LiCo}_{1/3}\text{Ni}_{1/3}\text{Mn}_{1/3}\text{O}_2$  modified by  $\text{CeO}_2$ -coating. *Electrochim. Acta* **2009**, *54*, 6803–6807. [[CrossRef](#)]
15. McNulty, R.C.; Hampson, E.; Cutler, L.N.; Grey, C.P.; Dose, W.M.; Johnson, L.R. Understanding the limits of Li-NMC811 half-cells. *J. Mater. Chem. A* **2023**, *11*, 18302–18312. [[CrossRef](#)]
16. Bianchini, M.; Roca-Ayats, M.; Hartmann, P.; Brezesinski, T.; Janek, J. There and Back Again—The Journey of  $\text{LiNiO}_2$  as a Cathode Active Material. *Angew. Chem. (Int. Ed. Engl.)* **2019**, *58*, 10434–10458. [[CrossRef](#)]
17. Ceder, G.; Doyle, M.; Arora, P.; Fuentes, Y. Computational Modeling and Simulation for Rechargeable Batteries. *MRS Bull.* **2002**, *27*, 619–623. [[CrossRef](#)]

18. Bhatt, M.D.; O'Dwyer, C. Recent progress in theoretical and computational investigations of Li-ion battery materials and electrolytes. *Phys. Chem. Chem. Phys.* **2015**, *17*, 4799–4844. [[CrossRef](#)]
19. Fallahzadeh, R.; Farhadian, N. Molecular dynamics simulation of lithium ion diffusion in LiCoO<sub>2</sub> cathode material. *Solid State Ion.* **2015**, *280*, 10–17. [[CrossRef](#)]
20. Haruyama, J.; Sodeyama, K.; Tateyama, Y. Cation Mixing Properties toward Co Diffusion at the LiCoO<sub>2</sub> Cathode/Sulfide Electrolyte Interface in a Solid-State Battery. *ACS Appl. Mater. Interfaces* **2017**, *9*, 286–292. [[CrossRef](#)]
21. Hüger, E.; Schmidt, H. Li Chemical and Tracer Diffusivities in LiCoO<sub>2</sub> Sintered Pellets. *Batteries* **2024**, *10*, 446. [[CrossRef](#)]
22. Islam, M.S.; Fisher, C.A.J. Lithium and sodium battery cathode materials: Computational insights into voltage, diffusion and nanostructural properties. *Chem. Soc. Rev.* **2014**, *43*, 185–204. [[CrossRef](#)]
23. Urban, A.; Seo, D.-H.; Ceder, G. Computational understanding of Li-ion batteries. *NPJ Comput. Mater.* **2016**, *2*, 1126. [[CrossRef](#)]
24. van der Ven, A.; Bhattacharya, J.; Belak, A.A. Understanding Li diffusion in Li-intercalation compounds. *Acc. Chem. Res.* **2013**, *46*, 1216–1225. [[CrossRef](#)]
25. Amin, R.; Chiang, Y.-M. Characterization of Electronic and Ionic Transport in Li<sub>1-x</sub>Ni<sub>0.33</sub>Mn<sub>0.33</sub>Co<sub>0.33</sub>O<sub>2</sub> (NMC 333) and Li<sub>1-x</sub>Ni<sub>0.50</sub>Mn<sub>0.20</sub>Co<sub>0.30</sub>O<sub>2</sub> (NMC 523) as a Function of Li Content. *J. Electrochem. Soc.* **2016**, *163*, A1512–A1517. [[CrossRef](#)]
26. Wu, S.-L.; Zhang, W.; Song, X.; Shukla, A.K.; Liu, G.; Battaglia, V.; Srinivasan, V. High Rate Capability of Li(Ni<sub>1/3</sub>Mn<sub>1/3</sub>Co<sub>1/3</sub>)O<sub>2</sub> Electrode for Li-Ion Batteries. *J. Electrochem. Soc.* **2012**, *159*, A438. [[CrossRef](#)]
27. Li, X.; Liu, J.; Banis, M.N.; Lushington, A.; Li, R.; Cai, M.; Sun, X. Atomic layer deposition of solid-state electrolyte coated cathode materials with superior high-voltage cycling behavior for lithium ion battery application. *Energy Environ. Sci.* **2014**, *7*, 768–778. [[CrossRef](#)]
28. Zheng, W.; Shui, M.; Shu, J.; Gao, S.; Xu, D.; Chen, L.; Feng, L.; Ren, Y. GITT studies on oxide cathode LiNi<sub>1/3</sub>Co<sub>1/3</sub>Mn<sub>1/3</sub>O<sub>2</sub> synthesized by citric acid assisted high-energy ball milling. *Bull. Mater. Sci.* **2013**, *36*, 495–498. [[CrossRef](#)]
29. Charbonneau, V.; Lasia, A.; Brisard, G. Impedance studies of Li<sup>+</sup> diffusion in nickel manganese cobalt oxide (NMC) during charge/discharge cycles. *J. Electroanal. Chem.* **2020**, *875*, 113944. [[CrossRef](#)]
30. Kang, S.D.; Kuo, J.J.; Kapate, N.; Hong, J.; Park, J.; Chueh, W.C. Galvanostatic Intermittent Titration Technique Reinvented: Part II. Experiments. *J. Electrochem. Soc.* **2021**, *168*, 120503. [[CrossRef](#)]
31. Tsai, P.-C.; Wen, B.; Wolfman, M.; Choe, M.-J.; Pan, M.S.; Su, L.; Thornton, K.; Cabana, J.; Chiang, Y.-M. Single-particle measurements of electrochemical kinetics in NMC and NCA cathodes for Li-ion batteries. *Energy Environ. Sci.* **2018**, *11*, 860–871. [[CrossRef](#)]
32. Mehrer, H. *Diffusion in Solids. Fundamentals, Methods, Materials, Diffusion-Controlled Processes*, 1st ed.; Springer Series in Solid-State Sciences; Springer: Berlin/Heidelberg, Germany; New York, NY, USA, 2007; Volume 155, ISBN 978-3-540-71486-6.
33. Maier, J. *Physical Chemistry of Ionic Materials: Ions and Electrons in Solids*, 1st ed.; John Wiley & Sons: Chichester, UK, 2004; Print ISBN 9780471999911, Online ISBN 9780470020227. [[CrossRef](#)]
34. Maier, J. On the correlation of macroscopic and microscopic rate constants in solid state chemistry. *Solid State Ion.* **1998**, *112*, 197–228. [[CrossRef](#)]
35. Maier, J. Mass Transport in the Presence of Internal Defect Reactions—Concept of Conservative Ensembles: I, Chemical Diffusion in Pure Compounds. *J. Am. Ceram. Soc.* **1993**, *76*, 1212–1217. [[CrossRef](#)]
36. Hüger, E.; Schmidt, H. Lithium tracer diffusion in ion-beam sputtered nano-crystalline and amorphous LiNi<sub>0.33</sub>Mn<sub>0.33</sub>Co<sub>0.33</sub>O<sub>2</sub> films. *Solid State Ion.* **2024**, *417*, 116702. [[CrossRef](#)]
37. Cho, S.; Uddin, M.; Alaboina, P.; Han, S.; Nandasiri, M.; Choi, Y.; Hu, E.; Nam, K.; Schwarz, A.; Nune, S.; et al. Exploring Lithium Deficiency in Layered Oxide Cathode for Li-Ion Battery. *Adv. Sustain. Syst.* **2017**, *1*, 1700026. [[CrossRef](#)]
38. Cho, S.; Chung, C.; Podowitz-Thomas, S.; Jones, J. Understanding the lithium deficient Li<sub>x</sub>Ni<sub>y</sub>Mn<sub>z</sub>Co<sub>1-y-z</sub>O<sub>2</sub> (x < 1) cathode materials structure. *Mater. Chem. Phys.* **2019**, *228*, 32–36. [[CrossRef](#)]
39. Lu, X.; Sun, Y.; Jian, Z.; He, X.; Gu, L.; Hu, Y.; Li, H.; Wang, Z.; Chen, W.; Duan, X.; et al. New Insight into the Atomic Structure of Electrochemically Delithiated O<sub>3</sub>-Li<sub>(1-x)</sub>CoO<sub>2</sub> (0 ≤ x ≤ 0.5) Nanoparticles. *Nano Lett.* **2012**, *12*, 6192–6197. [[CrossRef](#)]
40. Arai, H. Reversibility of LiNiO<sub>2</sub> cathode. *Solid State Ion.* **1997**, *95*, 275–282. [[CrossRef](#)]
41. Dahn, J.R.; von Sacken, U.; Michal, C.A. Structure and electrochemistry of Li<sub>1±y</sub>NiO<sub>2</sub> and a new Li<sub>2</sub>NiO<sub>2</sub> phase with the Ni(OH)<sub>2</sub> structure. *Solid State Ion.* **1990**, *44*, 87–97. [[CrossRef](#)]
42. Rossen, E.; Reimers, J.; Dahn, J. Synthesis and electrochemistry of spinel LT-LiCoO<sub>2</sub>. *Solid State Ion.* **1993**, *62*, 53–60. [[CrossRef](#)]
43. Antaya, M.; Dahn, J.; Preston, J.; Rossen, E.; Reimers, J. Preparation and Characterization of LiCoO<sub>2</sub> Thin Films by Laser Ablation Deposition. *J. Electrochem. Soc.* **1993**, *140*, 575–578. [[CrossRef](#)]
44. Antaya, M.; Cearn, K.; Preston, J.; Reimers, J.; Dahn, J. In situ growth of layered, spinel, and rock-salt LiCoO<sub>2</sub> by laser ablation deposition. *J. Appl. Phys.* **1994**, *76*, 2799–2806. [[CrossRef](#)]
45. Whitfield, P.S.; Davidson, I.J.; Cranswick, L.M.D.; Swainson, I.P.; Stephens, P.W. Investigation of possible superstructure and cation disorder in the lithium battery cathode material LiMn<sub>1/3</sub>Ni<sub>1/3</sub>Co<sub>1/3</sub>O<sub>2</sub> using neutron and anomalous dispersion powder diffraction. *Solid State Ion.* **2005**, *176*, 463–471. [[CrossRef](#)]

46. Shaju, K.M.; Bruce, P.G. Macroporous  $\text{Li}(\text{Ni}_{1/3}\text{Co}_{1/3}\text{Mn}_{1/3})\text{O}_2$ : A high-rate positive electrode for rechargeable lithium batteries. *J. Power Sources* **2007**, *174*, 1201–1205. [[CrossRef](#)]
47. Zhang, X.; Jiang, W.J.; Mauger, A.; Qilu; Gendron, F.; Julien, C. Minimization of the cation mixing in  $\text{Li}_{1+x}(\text{NMC})_{1-x}\text{O}_2$  as cathode material. *J. Power Sources* **2010**, *195*, 1292–1301. [[CrossRef](#)]
48. Wang, D.; Kou, R.; Ren, Y.; Sun, C.; Zhao, H.; Zhang, M.; Li, Y.; Huq, A.; Ko, J.; Pan, F.; et al. Synthetic Control of Kinetic Reaction Pathway and Cationic Ordering in High-Ni Layered Oxide Cathodes. *Adv. Mater.* **2017**, *29*, 1606715. [[CrossRef](#)]
49. Sun, G.; Yin, X.; Yang, W.; Song, A.; Jia, C.; Yang, W.; Du, Q.; Ma, Z.; Shao, G. The effect of cation mixing controlled by thermal treatment duration on the electrochemical stability of lithium transition-metal oxides. *Phys. Chem. Chem. Phys.* **2017**, *19*, 29886. [[CrossRef](#)]
50. Reynaud, M.; Casas-Cabanas, M. Order and disorder in NMC layered materials: A FAULTS simulation analysis. *Powder Diffr.* **2017**, *32*, S213–S220. [[CrossRef](#)]
51. Xiao, Y.; Liu, T.; Liu, J.; He, L.; Chen, J.; Zhang, J.; Luo, P.; Lu, H.; Wang, R.; Zhu, W.; et al. Insight into the origin of lithium/nickel ions exchange in layered  $\text{Li}(\text{Ni}_x\text{Mn}_y\text{Co}_z)\text{O}_2$  cathode materials. *Nano Energy* **2018**, *49*, 77–85. [[CrossRef](#)]
52. Kim, Y. Theoretical investigation of the cation antisite defect in layer-structured cathode materials for Li-ion batteries. *Phys. Chem. Chem. Phys.* **2019**, *21*, 24139. [[CrossRef](#)] [[PubMed](#)]
53. Zheng, J.; Ye, Y.; Liu, T.; Xiao, Y.; Wang, C.; Wang, F.; Pan, F. Ni/Li Disordering in Layered Transition Metal Oxide: Electrochemical Impact, Origin, and Control. *Acc. Chem. Res.* **2019**, *52*, 2201–2209. [[CrossRef](#)] [[PubMed](#)]
54. Park, H.; Mesnier, A.; Lee, S.; Jarvis, K.; Manthiram, A.; Warner, J.H. Intrinsic Li Distribution in Layered Transition-Metal Oxides Using Low-Dose Scanning Transmission Electron Microscopy and Spectroscopy. *Chem. Mater.* **2021**, *33*, 4638–4650. [[CrossRef](#)]
55. Orlova, E.D.; Savina, A.A.; Abakumov, S.A.; Morozov, A.V.; Abakumov, A.M. Comprehensive Study of  $\text{Li}^+/\text{Ni}^{2+}$  Disorder in Ni-Rich NMCs Cathodes for Li-Ion Batteries. *Symmetry* **2021**, *13*, 1628. [[CrossRef](#)]
56. Boev, A.O.; Fedotov, S.S.; Abakumov, A.M.; Stevenson, K.J.; Henkelman, G.; Aksyonov, D.A. The role of antisite defect pairs in surface reconstruction of layered AMO<sub>2</sub> oxides: A DFT+U study. *Appl. Surf. Sci.* **2021**, *537*, 147750. [[CrossRef](#)]
57. Wei, H.; Tang, L.; Huang, Y.; Wang, Z.; Luo, Y.; He, Z.; Yan, C.; Mao, J.; Dai, K.; Zheng, J. Comprehensive understanding of Li/Ni intermixing in layered transition metal oxides. *Mater. Today* **2021**, *51*, 365–392. [[CrossRef](#)]
58. Aksyonov, D.A.; Boev, A.O.; Fedotov, S.S.; Abakumov, A.M. Computational insights into ionic conductivity of transition metal electrode materials for metal-ion batteries—A review. *Solid State Ion.* **2023**, *393*, 116170. [[CrossRef](#)]
59. Tahmasebi, M.; Obrovac, M.N. Quantitative Measurement of Compositional Inhomogeneity in NMC Cathodes by X-ray Diffraction. *J. Electrochem. Soc.* **2023**, *170*, 080519. [[CrossRef](#)]
60. Fan, F.; Zeng, R.; Zheng, T.; Xu, H.; Wen, X.; Wang, X.; Tian, G.; Wang, S.; Zheng, C.; Wei, X.; et al. Cation-ordered Ni-rich positive electrode material with superior chemical and structural stability enabled by atomic substitution for lithium-ion batteries. *Chem. Eng. J.* **2023**, *477*, 147181. [[CrossRef](#)]
61. Ben-Barak, I.; Obrovac, M.N. All-Dry Synthesis of NMC from  $[\text{Ni},\text{Mn},\text{Co}]_3\text{O}_4$  Spinel Precursors. *J. Electrochem. Soc.* **2024**, *171*, 040535. [[CrossRef](#)]
62. Zeng, C.; Fan, F.; Zheng, R.; Wang, X.; Tian, G.; Liu, S.; Liu, P.; Wang, C.; Wang, S.; Shu, C. Structure and Charge Regulation Strategy Enabling Superior Cycling Stability of Ni-Rich Cathode Materials. *ACS Appl. Mater. Interfaces* **2024**, *16*, 11377–11388. [[CrossRef](#)]
63. Zeng, C.; Zheng, R.; Fan, F.; Wang, X.; Tian, G.; Liu, S.; Liu, P.; Wang, C.; Wang, S.; Shu, C. Phase compatible surface engineering to boost the cycling stability of single-crystalline Ni-rich cathode for high energy density lithium-ion batteries. *Energy Storage Mater.* **2024**, *72*, 103788. [[CrossRef](#)]
64. Lei, X.; Zhao, J.; Wang, J.; Su, D. Tracking lithiation with transmission electron microscopy. *Sci. China Chem.* **2024**, *67*, 291–311. [[CrossRef](#)]
65. Ceder, G.; Van der Ven, A. Phase diagrams of lithium transition metal oxides: Investigations from first principles. *Electrochim. Acta* **1999**, *45*, 131–150. [[CrossRef](#)]
66. Sharifi-Asl, S.; Lu, J.; Amine, K.; Shahbazian-Yassar, R. Oxygen Release Degradation in Li-Ion Battery Cathode Materials: Mechanisms and Mitigating Approaches. *Adv. Energy Mater.* **2019**, *9*, 1900551. [[CrossRef](#)]
67. Cho, Y.; Lee, S.; Lee, Y.; Hong, T.; Cho, J. Spinel-Layered Core-Shell Cathode Materials for Li-Ion Batteries. *Adv. Energy Mater.* **2011**, *1*, 821. [[CrossRef](#)]
68. Qiu, B.; Zhang, M.; Wu, L.; Wang, J.; Xia, Y.; Qian, D.; Liu, H.; Hy, S.; Chen, Y.; An, K.; et al. Gas–solid interfacial modification of oxygen activity in layered oxide cathodes for lithium-ion batteries. *Nat. Commun.* **2016**, *7*, 12108. [[CrossRef](#)] [[PubMed](#)]
69. Crank, J. *The Mathematics of Diffusion*; Oxford University Press: Oxford, UK, 1979.

70. Van der Ven, A.; Ceder, G. Lithium Diffusion in Layered  $\text{Li}_x\text{CoO}_2$ . *Electrochem. Solid-State Lett.* **2000**, *3*, 301. [[CrossRef](#)]
71. Hoang, K.; Johannes, M.D. Defect chemistry in layered transition-metal oxides from screened hybrid density functional calculations. *J. Mater. Chem. A* **2014**, *2*, 5224–5235. [[CrossRef](#)]

**Disclaimer/Publisher's Note:** The statements, opinions and data contained in all publications are solely those of the individual author(s) and contributor(s) and not of MDPI and/or the editor(s). MDPI and/or the editor(s) disclaim responsibility for any injury to people or property resulting from any ideas, methods, instructions or products referred to in the content.